



# AGILE Observations of the LIGO-Virgo Gravitational-wave Events of the GWTC-1 Catalog

A. Ursi<sup>1</sup>, F. Verrecchia<sup>2,3</sup>, G. Piano<sup>1</sup>, C. Casentini<sup>1,4</sup>, M. Tavani<sup>1,5</sup>, A. Bulgarelli<sup>6</sup>, M. Cardillo<sup>1</sup>, F. Longo<sup>7</sup>,  
F. Lucarelli<sup>2,3</sup>, A. Morselli<sup>4</sup>, N. Parmiggiani<sup>6</sup>, M. Pilia<sup>8</sup>, C. Pittori<sup>2,3</sup>, and A. Rappoldi<sup>9</sup>

<sup>1</sup> INAF/IAPS, via del Fosso del Cavaliere 100, I-00133 Roma (RM), Italy; [alessandro.ursi@inaf.it](mailto:alessandro.ursi@inaf.it)

<sup>2</sup> SSDC/ASI, via del Politecnico snc, I-00133 Roma (RM), Italy

<sup>3</sup> INAF/OAR, via Frascati 33, I-00078 Monte Porzio Catone (RM), Italy

<sup>4</sup> INFN Sezione di Roma 2, via della Ricerca Scientifica 1, I-00133 Roma (RM), Italy

<sup>5</sup> Università degli Studi di Roma Tor Vergata, via della Ricerca Scientifica 1, I-00133 Roma (RM), Italy

<sup>6</sup> INAF/OAS, via Gobetti 101, I-40129 Bologna (BO), Italy

<sup>7</sup> Dipartimento di Fisica, Università di Trieste and INFN, via Valerio 2, I-34127 Trieste (TR), Italy

<sup>8</sup> INAF—Osservatorio Astronomico di Cagliari, via della Scienza 5, I-09047 Selargius (CA), Italy

<sup>9</sup> INFN Sezione di Pavia, via Bassi 6, I-27100 Pavia (PV), Italy

Received 2021 September 16; revised 2021 October 22; accepted 2021 October 24; published 2022 January 13

## Abstract

We present a comprehensive review of AGILE follow-up observations of the Gravitational Wave (GW) events and the unconfirmed marginal triggers reported in the first LIGO-Virgo (LV) Gravitational Wave Transient Catalog (GWTC-1). For seven GW events and 13 LV triggers, the associated 90% credible region was partially or fully accessible to the AGILE satellite at the  $T_0$ ; for the remaining events, the localization region was not accessible to AGILE due to passages into the South Atlantic Anomaly, or complete Earth occultations (as in the case of GW170817). A systematic search for associated transients, performed on different timescales and on different time intervals about each event, led to the detection of no gamma-ray counterparts. We report AGILE MCAL upper limit fluences in the 400 keV–100 MeV energy range, evaluated in a time window of  $T_0 \pm 50$  s around each event, as well as AGILE GRID upper limit (UL) fluxes in the 30 MeV–50 GeV energy range, evaluated in a time frame of  $T_0 \pm 950$  s around each event. All ULs are estimated at different integration times and are evaluated within the portions of GW credible region accessible to AGILE at the different times under consideration. We also discuss the possibility of AGILE MCAL to trigger and detect a weak soft-spectrum burst such as GRB 170817A.

*Unified Astronomy Thesaurus concepts:* [Gamma-ray bursts \(629\)](#); [Gravitational waves \(678\)](#)

## 1. Introduction

The Advanced Laser Interferometer Gravitational Observatory (LIGO) and Advanced Virgo detectors are a ground-based network of interferometers, sensitive in the 15 Hz–few kHz frequency range, aimed at detecting Gravitational Wave (GW) events produced by the inspiral, merger, and ringdown of Compact Binary Coalescences (CBCs) (Acernese et al. 2015; LIGO Scientific Collaboration et al. 2015), as well as GWs from unmodeled transients and bursts, Continuous-Wave signals, and Stochastic GW Background (SGWB). This class includes stellar mass Binary Black Holes (BBHs), Neutron Star–black hole (NS–BH), and Binary Neutron Star (BNS) mergers.

The first Observing run (O1) of the Advanced LIGO (2015 September 12–2016 January 19) led to the detection of the first GW events from coalescing BBHs: GW150914 (Abbott et al. 2016a, 2016b, 2016c), and GW151226 (Abbott et al. 2016d). These detections started a new era in astronomy, opening a new way of studying compact binaries, testing general relativity in its strong regime, and investigating quantum properties of fields and matter. The second Observing run (O2) of Advanced LIGO (2016 November 30–2017 August 25) saw the participation of the Advanced Virgo (Acernese et al. 2015) detector (which joined 2017 August 1) and ended up with the detection of three new GW events produced by BBH mergers, GW170104 (Abbott et al. 2017a),

GW170608 (Abbott et al. 2017b), and GW170814 (Abbott et al. 2017c), as well as the first event produced by a BNS merger, GW170817 (Abbott et al. 2017d, 2017e, 2017f). In particular, the addition of Advanced Virgo substantially improved the sky localization of this GW source. This was fundamental to associate GW170817 to the Gamma-Ray Burst (GRB) 170817A, which occurred about  $\sim 1.7$  s after the GW  $T_0$  and was detected by Fermi GBM and INTEGRAL SPI (Savchenko et al. 2017; Goldstein et al. 2017): this detection provided the first confirmation of BNS mergers as progenitors of short GRBs, representing the first multimessenger observation of a CBC event.

### 1.1. The LIGO-Virgo First Gravitational Wave Transient Catalog (GWTC-1)

Abbott et al. (2019) presented an offline reanalysis of the data acquired during the O1 and O2 runs, in light of the improved O2 search pipelines, taking into consideration an expanded parameter space and data cleaning procedures. A refined analysis adopting two modeled matched-filter searches (PyCBC and GstLAL) and one unmodeled burst search for short-duration transients (coherent WaveBurst, cWB) ended up with 11 GW events. For what concerns O1, the LVT151012 event was promoted to gravitational wave GW151012, while for what concerns O2, four new previously unpublished GW events were announced: GW170809 and GW170823 (identified in low-latency by online pipelines and for which an automatic alert was sent to observing partners during the O2 run), and GW170729 and GW170818 (identified only in the offline analyses and

previously not released to electromagnetic observers). The GWTC-1 catalog also reports a sample of 14 LV triggers, which exhibit False Alarm Rate (FAR)  $< 1/30$  days in only one of the two matched-filter analyses, representing candidates whose astrophysical origin cannot be unambiguously confirmed nor excluded.

Recently, a second GWTC-2 catalog has been released, covering the LV observations of CBCs in the first half of the third run, O3a (2019 April 1–2019 October 1) (Abbott et al. 2021). This catalog includes candidate GW events, 13 of which were reported for the first time. The O3 run is of particular interest, as it contains the first-ever detected GW events from a neutron star–black hole binaries (NSBH).

### 1.2. AGILE and Gravitational Waves

During the O1 run of Advanced LIGO, AGILE was not part of the LIGO-Virgo (LV) follow-up multimessenger collaboration: an extensive study of the first detected event GW150914, searching for possible electromagnetic (EM) counterparts in the AGILE data, was carried out only after the event became public (Tavani et al. 2016). Despite not detecting any associated significant EM signal, AGILE provided the closest observation in time of the GW localization region, which was accessed within one minute from the event time, allowing to obtain a  $3\sigma$  flux upper limit of  $1.2 \times 10^{-8}$  erg cm $^{-2}$  s $^{-1}$  in the 50 MeV–10 GeV energy range.

During the O2 run of the Advanced LIGO and Advanced Virgo detectors, AGILE was an active EM partner for prompt follow-up observations. For the entire duration of the run, AGILE promptly reacted to the 14 alerts sent by the LIGO-Virgo collaboration, delivering a total number of 31 GCNs. A detailed study of the AGILE data was carried out in the case of GW170104 (Verrecchia et al. 2017b), for which a  $\sim 32$  ms duration signal was detected in the 0.4–100 MeV energy range about 0.46 s before the GW time, with a post-trial significance of  $\sim 2.6\sigma$ . For what concerns GW170817, the credible region was not accessible to AGILE at  $T_0$ , due to a complete Earth occultation that prevented any detection of the associated GRB 170817A (Verrecchia et al. 2017a). AGILE collected useful data preceding and following the burst time, constraining precursor, and delayed emission properties of the BNS coalescence event. In all the other cases, involving only BBH events and successively rejected triggers, AGILE did not detect any significant EM counterpart associated with the event alerts sent by the LV collaboration throughout the O2 run but provided gamma-ray upper limits. A review of the AGILE search for gamma-ray counterparts of GW events is provided by Verrecchia et al. (2019). This study was performed on the events reported during the O1 and O2 runs before the offline reanalysis by LV presented in the GWTC-1, and the release of improved contour regions and new GW events and triggers. Successively, AGILE actively participated in the LV O3 follow-up campaign, from 2019 April 1 to 2020 March 27.<sup>10</sup>

The search for EM signatures of GW events is extremely important, as the detection or nondetection of associated EM emission could help to shed light on the formation and evolution of CBCs, providing insights into the properties of compact objects. However, the large sky localization uncertainty regions typically provided by LV (up to thousands of

**Table 1**  
Main Specifics of the AGILE MCAL and GRID Detectors

	MCAL	GRID
Energy range	400 keV–100 MeV	30 MeV–50 GeV
Field of view	$4\pi$ sr (nonimaging)	2.5 sr
Effective area	300 cm $^2$ @ 1 MeV	500 cm $^2$ @ 1 GeV
Absolute time resolution	4 $\mu$ s	2 $\mu$ s
Dead time	20 $\mu$ s	100–200 $\mu$ s
Angular resolution	...	1 $^\circ$ 2 @ 400 MeV

square degrees) in O1 and most of O2, as well as the non-negligible Earth occultations of portions of the localization regions and the repeated passages into the South Atlantic Anomaly (SAA), where low-Earth orbit satellites are not operative, make this search rather challenging.

In this work, we focus on the events reported in the GWTC-1 catalog concerning the O1 and O2 observational runs, as they represent a comprehensive sample, obtained after an offline revision with further analyses involving different updated pipelines. A similar study will be carried out when the second catalog of LV events acquired during the O3 run will be released by the collaboration.

## 2. The AGILE Satellite

The AGILE satellite (Tavani et al. 2009) is an Italian satellite devoted to high-energy astrophysics composed by an imaging gamma-ray Silicon Tracker (ST; 30 MeV–50 GeV), a coded mask X-ray imager Super-AGILE (SA, 20–60 keV), a nonimaging Mini-CALorimeter (MCAL; 400 keV–100 MeV), and an Anti-Coincidence system (AC; 50–200 keV). The suite of ST, MCAL, and AC detectors working together form the so-called Gamma-Ray Imaging Detector (GRID) (Barbiellini et al. 2002; Prest et al. 2003). AGILE currently orbits at an altitude of  $\sim 500$  km, in a  $\pm 2.5^\circ$  quasi-equatorial orbit, spinning about its axis in about 7 minutes and monitoring 80% of the sky with its imaging detectors. Satellite data are transmitted to the ground at every passage over the ASI Ground Station in Malindi, Kenya, and successively processed by fast processing at the AGILE data center in ASI-SSDC (Pittori & The Agile-Ssdc Team 2019), producing alerts for transient gamma-ray sources within 20 minutes–2 hr from the satellite onboard acquisition. Tavani (2019) provides a global review on the main scientific results and contributions of the AGILE mission during its more than ten-year lifetime.

In this work, we focus on the analysis of the AGILE MCAL and AGILE GRID data, which are illustrated in detail in the following sections, and whose main specifics are reported in Table 1.

### 2.1. The AGILE MCAL and MCAL Trigger Logic

Different from the imaging detectors onboard AGILE, MCAL (Marisaldi et al. 2008; Labanti et al. 2009) is an all-sky monitor composed of 30 CsI(Tl) scintillation bars, that provide a total on-axis geometrical area of 1400 cm $^2$ . MCAL is capable of detecting gamma-ray transients, such as both long and short GRBs (Giuliani et al. 2008, 2010; Del Monte et al. 2009, 2011; Galli et al. 2013; Ursi et al. 2021). Its onboard

<sup>10</sup> All published AGILE O3 follow-up results have been grouped at [https://agile.ssdsc.asi.it/news\\_gw.html](https://agile.ssdsc.asi.it/news_gw.html).

trigger logic works on seven different timescales: 0.293, 1, 16, 64, 256, 1024, and 8192 ms. The 0.293 ms (or submillisecond) timescale represents a key feature of the AGILE satellite, which allows detecting short-duration impulsive events such as very short GRBs (e.g., GRB 090522; Ursi et al. 2021) and Terrestrial Gamma-ray Flashes, TGFs (Marisaldi et al. 2010, 2014; Maiorana et al. 2020). The MCAL onboard trigger logic configuration was modified for the LV O2 and O3 GW observational campaigns from a “BASELINE” configuration to an “MCAL-GW” configuration. This was performed to enhance the detector trigger capabilities to reveal short-duration gamma-ray events and to enlarge the total onboard exposure time of MCAL (Ursi et al. 2019).

Once MCAL data are downloaded, an offline algorithm performs a blind search for signatures of impulsive transients (i.e., GRBs, TGFs, subthreshold events) within each MCAL trigger acquisition. Moreover, the AGILE team has developed various automatic pipelines to carry out quick analysis of MCAL data, after each satellite ground contact. The main goal of these pipelines is the offline detection and prompt communication of fast transients to the AGILE Team and to the scientific community via the delivery of automatic Gamma-ray Coordinates Network (GCN) Notices. These pipelines also perform rapid follow-up of external alerts, in the multiwavelength and multimessenger context, allowing the AGILE team to promptly react to LV GW alerts (Bulgarelli 2019a, 2019b).

## 2.2. The AGILE GRID

The AGILE GRID is a pair-production telescope with 12 planes of Si strip detectors, the first 10 of which lie under a pair-conversion tungsten layer (Barbiellini et al. 2002). GRID is characterized by a fine spatial resolution (obtained by a special arrangement of Si microstrip detectors and analog signal storage and processing) and by the smallest ever obtained dead time for gamma-ray detection ( $\leq 200 \mu\text{s}$ ). Charged particles are tracked by Si microstrip detectors configured to provide two orthogonal coordinates for every single element. The AGILE GRID has a very large field of view (FOV) of (2.5 sr), with  $\sim 80\%$  of the whole sky that can be monitored every 7 minutes due to the satellite spinning. Its sensitivity is on the order of  $\sim 10^{-8} \text{ erg cm}^{-2} \text{ s}^{-1}$  above 30 MeV, for typical single-pass of unocculted sky regions, with a good angular resolution ( $\sim 1^\circ\text{--}2^\circ$  in the 400 MeV–1 GeV) quite uniform up to  $30^\circ$  off-axis. GRID data analysis is also included in the automatic pipeline system for the rapid follow-up of external alerts, providing continuous monitoring of the available FOV in a large time interval about the alert time.

## 3. AGILE Observations of the GWTC-1 Events

First of all, we checked how many GW events were accessible to the AGILE satellite at the  $T_0$ , that is, events for which the associated LV 90% credible region (i.e., the sky localization defined as the area of the sky including a given total posterior probability) was accessible to the AGILE detectors. Such “accessibility” is different depending on the detector. As MCAL is an all-sky monitor, the limitation of its ideal  $4\pi$  FOV is only given by Earth occultation. As a consequence, the portions of the accessible credible region only depend on the position of the satellite with respect to the Earth and to the localization region. On the other hand, for imaging detectors such as GRID and Super-AGILE, the portions of GW

contour regions accessible to their FOVs depend also on the off-axis angle with respect to the localization region. As the satellite spins around its Sun-pointing axis, the fractions of contour regions accessible to AGILE vary in time and should be evaluated at each time interval.

We reconstructed the attitude of AGILE at each GW  $T_0$  in order to evaluate the percentage of accessible contour regions. We also verified whether the satellite was passing into the SAA, where all detectors are usually switched off and no data are acquired. For the marginal triggers, no credible regions are provided by LV. As a consequence, if the satellite was not passing into the SAA region, the percentage of LV localization region accessible to AGILE simply corresponds to the fraction of sky not suffering Earth occultation, which is constantly equal to about  $\sim 65\%$  of the sky.

Table 2 shows that, for GW150914, GW151012, GW151226, GW170104, GW170608, GW170729, and GW170809, the related credible regions were accessible to AGILE (in six of these cases, more than  $3/4$  of the total credible region was accessible at the  $T_0$ ). On the other hand, for GW170814 and GW170817, no observation of the events was possible due to complete Earth occultation of the associated credible regions, whereas for GW170818 and GW170823, no MCAL analysis was possible due to ongoing passages into the SAA. The occultation of GW170817 prevented any possible detection of the associated GRB 170817A as well. Similarly, LV triggers are all accessible to AGILE, except for 151008, which took place during a passage into the SAA.

### 3.1. AGILE MCAL Observations

As illustrated in Section 3, the limitation of MCAL FOV to the LV localization regions only depends on Earth occultation only, and the GW events accessible to MCAL are therefore those accessible to the AGILE satellite itself.

In order to investigate the existence of possible EM GW counterparts detected by MCAL, we searched for MCAL triggers within  $T_0 \pm 50$  s about each event. Such window was adopted considering that possible CBC-associated short GRB emissions are expected to occur from tens of ms to a few seconds from the GW event (Zhang 2019), and to consider a sufficiently large interval to investigate possible precursive or delayed emissions. Figure 1 shows the geographic longitude distribution of MCAL onboard triggers acquired within a complete AGILE orbit, centered at  $T_0$ , for GW170608. Each trigger is represented by a red vertical stripe, whose width corresponds to the duration of the related data acquisition, and the blue central strip represents the  $T_0 \pm 50$  s time window in which the search for possible signals was carried out. The green region schematically represents the geographic position of the SAA, where all detectors are switched off.

### 3.2. AGILE MCAL Triggers

As used in other contexts of different searches for external transients data analysis (e.g., for Fast Radio Bursts), the triggered data acquisitions are investigated in two ways. The first approach is to identify the signal that issued the trigger in order to evaluate its signal-to-noise ratio (S/N), triggered timescale, and corresponding FAR. As pointed out in Section 2.1, the majority of onboard triggers are ascribed to electronic noise and charged particles crossing the detector and it is therefore important to carry out a detailed analysis to

**Table 2**  
List of the 11 GW Events and of the 14 LV Marginal Triggers Reported in the GWTC-1 Catalog

GW Event	Type	$d_L$ / Mpc	$z$	$E_{\text{rad}}/(M_{\odot}c^2)$	Unocculted Fraction of GW Credible Region at $T_0$	Accessible to AGILE at $T_0$
GW150914	BBH	$430^{+150}_{-170}$	$0.09^{+0.03}_{-0.03}$	$3.1^{+0.4}_{-0.4}$	80%	yes
GW151012	BBH	$1060^{+540}_{-480}$	$0.21^{+0.09}_{-0.09}$	$1.5^{+0.5}_{-0.5}$	80%	yes
GW151226	BBH	$440^{+180}_{-190}$	$0.09^{+0.04}_{-0.04}$	$1.0^{+0.1}_{-0.2}$	75%	yes
GW170104	BBH	$960^{+430}_{-410}$	$0.19^{+0.07}_{-0.08}$	$2.2^{+0.5}_{-0.5}$	90%	yes
GW170608	BBH	$320^{+120}_{-110}$	$0.07^{+0.02}_{-0.02}$	$0.9^{+0.0}_{-0.1}$	20%	yes
GW170729	BBH	$2750^{+1350}_{-1320}$	$0.48^{+0.19}_{-0.20}$	$4.8^{+1.7}_{-1.7}$	75%	yes
GW170809	BBH	$990^{+320}_{-380}$	$0.20^{+0.05}_{-0.07}$	$2.7^{+0.6}_{-0.6}$	100%	yes
GW170814	BBH	$580^{+160}_{-210}$	$0.12^{+0.03}_{-0.04}$	$2.7^{+0.4}_{-0.3}$	0%	no (total Earth occultation)
GW170817	BNS	$40^{+10}_{-10}$	$0.01^{+0.00}_{-0.00}$	$\geq 0.04$	0%	no (total Earth occultation)
GW170818	BBH	$1020^{+430}_{-360}$	$0.20^{+0.07}_{-0.07}$	$2.7^{+0.5}_{-0.5}$	100%	no (passage into SAA)
GW170823	BBH	$1850^{+840}_{-840}$	$0.34^{+0.13}_{-0.14}$	$3.3^{+0.9}_{-0.8}$	45%	no (passage into SAA)
LV trigger	search pipeline		$M_{\text{det}} [M_{\odot}]$		unocculted fraction of GW credible region at $T_0$	accessible to AGILE at $T_0$
151008	PyCBC		5.12		65%	no (passage into SAA)
151012A	GstLAL		2.01		65%	yes
151116	PyCBC		1.24		65%	yes
161202	PyCBC		1.54		65%	yes
161217	GstLAL		7.86		65%	yes
170208	GstLAL		7.39		65%	yes
170219	GstLAL		1.53		65%	yes
170405	GstLAL		1.44		65%	yes
170412	GstLAL		4.36		65%	yes
170423	GstLAL		1.17		65%	yes
170616	PyCBC		2.75		65%	yes
170630	GstLAL		0.90		65%	yes
170705	GstLAL		3.40		65%	yes
170720	GstLAL		5.96		65%	yes

**Note.** GW events are shown with related classification, distance, redshift, and radiated energy, whereas triggers are shown with the corresponding pipeline search which identified them, and the most significant template chirp mass obtained from that search. For each event, we report the percentage of 90% credible region unocculted by the Earth at the  $T_0$  and information about the accessibility of the event to the AGILE satellite (as marginal triggers do not have a credible region, the corresponding accessible region is constantly equal to about 65% of the sky).

rule out such signals. The second approach is to carry out a blind search for transients throughout the whole data stream acquired by each MCAL trigger within  $\pm 50$  s, independently on the MCAL trigger time. For this step, we applied the same archival detection algorithm adopted for the automatic MCAL pipeline system that searches for signals with significances  $> 3\sigma$  over four different timescales (Ursi et al. 2019).

Table 3 shows triggered data acquisitions present within  $T_0 \pm 50$  s for four GW events and for nine LV marginal triggers. As these MCAL data acquisitions are issued on different logic timescales (in particular, on the submillisecond and 16 ms timescales), they have different durations. It is interesting to

notice that GW170104 and 170412 are the only events for which the MCAL data acquisitions completely cover their  $T_0$ s, while GW170608 is the event with the largest exposure around a GW (i.e.,  $\sim 40$  s). In all other cases, no MCAL triggers are present within  $T_0 \pm 50$  s, although the GW was fully or partially accessible to the AGILE satellite.

We investigated the signals that issued these triggers, carrying out statistical analysis to establish whether their proximity to the GW times might be statistically ascribed to chance coincidences and to evaluate the corresponding post-trial probability  $P$  that these events are actually associated. In order to quantitatively evaluate the null hypothesis that these

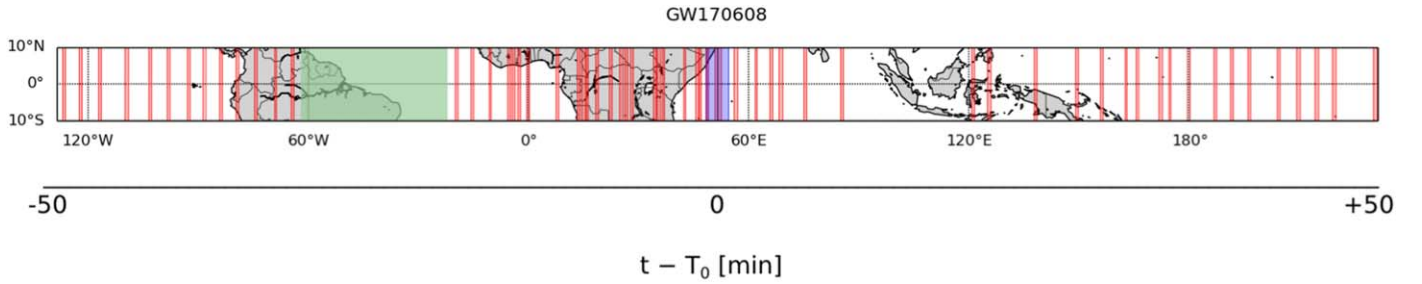


**Figure 1.** Geographic longitude distribution of MCAL triggers (red vertical strips) occurring within one AGILE orbit around GW170608. The blue central strip corresponds to the time window of  $T_0 \pm 50$  s considered for the search for counterparts, whereas the green region represents the SAA, where AGILE detectors are switched off. GW170608 represents the event with the largest MCAL exposure around the  $T_0$ .

events accidentally occur within a time interval  $\delta t$  from the GW events, we adopt the formalism already used by Connaughton et al. (2016) and Verrecchia et al. (2017b), where the post-trial probability is defined as:

$$P = N \cdot \text{FAR} \cdot \delta t \cdot \left[ 1 + \ln \left( \frac{\Delta t}{t_{\text{bin}}} \right) \right] \quad (1)$$

with  $N$  the number of trials, FAR the false alarm rate of the detected signal,  $\delta t$  the delay between  $T_0$  and the detected signal,  $\Delta t$  the one-sided time search window, and  $t_{\text{bin}}$  the timescale under analysis. We use a factor  $N = 7$  to account for the seven independent MCAL trigger logic timescales. The signals that issued MCAL triggers do not show significant excesses of counts with respect to the threshold values required to start an acquisition in the corresponding logic timescales. As a consequence, the FARs simply consist in the FARs of the trigger timescales, evaluated in a time interval of 2 weeks around the  $T_0$ : for the involved logics, we obtain  $\text{FAR}_{\text{subms}} \sim 2 \times 10^{-3}$  Hz and  $\text{FAR}_{16 \text{ ms}} \sim 5 \times 10^{-3}$  Hz. Finally, we evaluate the temporal offset  $t - T_0$  of each event from the corresponding GW  $T_0$ . In all cases, the resulting post-trial probability indicates that these triggers are completely consistent with chance coincidences. All parameters and corresponding probabilities are reported in Table 3. We conclude that the first approach pointed out that all the triggers found in close temporal association to the GW  $T_0$ s can be ascribed to a spurious origin.

The second approach, a blind search in the triggered data acquisitions, allows to identify only one signal that can be associated with GW170104, detected at  $T_0 + 0.46$  s in the  $t_{\text{bin}} = 32$  ms timescale with the pre-trial significance of  $4.4\sigma$ . In this case, taking into consideration the related FAR of such signal and its temporal offset from the GW  $T_0$ , a post-trial probability of  $\sim 2.6\sigma$  is obtained. Detailed analysis of this event is already reported in Verrecchia et al. (2017b). In all other cases, no significant signals with  $S/N \geq 3\sigma$  have been found by the blind search.

### 3.2.1. AGILE MCAL Upper Limits

Table 4 reports fluence Upper Limits (ULs) for the seven GW events and 13 LV triggers accessible to AGILE MCAL at each  $T_0$ . The complete evaluation of MCAL UL fluences depends on many parameters: the background rate (which for these events varies from  $\sim 500$  to  $\sim 660$  Hz), the instrumental response matrix (which depends on the off-axis angle, evaluated on a set of 96 different satellite configurations), the

energy range under analysis (here, 400 keV–100 MeV), the spectral models used to simulate the event (here, three different models), the time interval on which the flux UL is integrated (which is 1 s if data are present at the  $T_0$ , or which corresponds to the seven trigger logic timescales if no trigger was issued), and the MCAL onboard configuration (“BASELINE” or “MCAL-GW”). Depending on these parameters, MCAL can reach different sensitivities, i.e., different minimum detectable fluences. In particular, ULs are evaluated for a  $1^\circ \times 1^\circ$  grid of celestial positions within each GW credible region, in the 400 keV–100 MeV energy range. The range of celestial positions considered inside the localization region corresponds to different angles with respect to the satellite boresight and to different MCAL response matrices. Given the typically large localization regions provided by LV, the evaluation of ULs is performed on a large set of celestial coordinates, leading to a range of UL values, from  $\text{UL}_{\text{min}}$  (more on-axis configuration, best sensitivity, and lower detectable fluences) to  $\text{UL}_{\text{max}}$  (less on-axis configuration, worst sensitivity, and higher detectable fluences). We adopted three spectral models to simulate the fluences needed to trigger the detector: model A, a single power-law model with photon index  $\beta = -1.4$ , as the Fermi GBM weak signal found in close temporal association to BBH GW150914 (Connaughton et al. 2016); model B, a single power-law model with photon index  $\beta = -2.3$  representing the average spectrum obtained for AGILE MCAL short GRBs sample (Ursi et al. 2021); and model C, a “comptonized” model, consisting of a power law with photon index  $\beta = -0.62$  and an exponential cutoff with peak energy  $E_p = 185$  keV, as the spectrum of GRB 170817A detected by Fermi GBM (Goldstein et al. 2017). Table 5 reports the models used for the UL evaluation. Finally, depending on whether the MCAL data cover the event  $T_0$  or not, fluxes ULs are integrated at different time intervals. In particular, if MCAL data are covering the  $T_0$  due to a data acquisition triggered by some spurious event (GW170104 and 170412), ULs are estimated as  $2\sigma$  UL fluences, integrated on 1 s.

Figure 2 shows a Mollweide projection of MCAL UL fluences for GW170104 and for marginal trigger 170412, where the GW90% credible region is represented in black (for GW170104) and the Earth is represented in gray. In Table 4, these ULs are marked with an asterisk. For completeness, we show also the AGILE boresight as a red dot, oriented along the satellite pointing direction. In the plot, we report only fluence data obtained for the spectral model B. If no MCAL data are available at the  $T_0$  (GW150914, GW151012, GW151012, GW170608, GW170729, GW170809, 151012A, 151116, 161202, 161217, 170208, 170219, 170405, 170423, 170616, 170630, 170705, and 170720), we carry out an independent

**Table 3**  
List of MCAL Triggers within  $T_0 \pm 50$  s about each Accessible GW and LV Marginal Trigger

GW Event	Signal Label	Trigger Start	Trigger Stop	S/N	$t_{\text{bin}}$	FAR (Hz)	$t - T_0$	FAP
GW150914	...	...	...	...	...	...	...	...
GW151012	...	...	...	...	...	...	...	...
GW151226	...	...	...	...	...	...	...	...
GW170104*	<i>trigger a</i>	$T_0 - 11.2$ s	$T_0 + 1.4$ s	$<3\sigma$	16 ms	$5 \times 10^{-3}$	-6.7 s	$>1$
	<i>signal i</i>			$4.4\sigma$	32 ms	$1 \times 10^{-4}$	+0.46 s	0.01 ( $\sim 2.6\sigma$ )
GW170608	<i>trigger a</i>	$T_0 - 53.3$ s	$T_0 - 40.5$ s	$<3\sigma$	16 ms	$5 \times 10^{-3}$	-48.4 s	$>1$
	<i>trigger b</i>	$T_0 - 14.4$ s	$T_0 - 0.1$ s	$<3\sigma$	0.3 ms	$2 \times 10^{-3}$	-10.3 s	$>1$
	<i>trigger c</i>	$T_0 + 2.0$ s	$T_0 + 15.3$ s	$<3\sigma$	0.3 ms	$2 \times 10^{-3}$	+6.5 s	$>1$
GW170729	<i>trigger a</i>	$T_0 + 29.2$ s	$T_0 + 44.9$ s	$<3\sigma$	16 ms	$5 \times 10^{-3}$	+33.6 s	$>1$
	<i>trigger b</i>	$T_0 + 48.8$ s	$T_0 + 60.3$ s	$<3\sigma$	0.3 ms	$2 \times 10^{-3}$	+53.3 s	$>1$
GW170809	<i>trigger a</i>	$T_0 + 8.3$ s	$T_0 + 22.6$ s	$<3\sigma$	16 ms	$5 \times 10^{-3}$	+13.3 s	$>1$
	<i>trigger b</i>	$T_0 + 30.8$ s	$T_0 + 46.2$ s	$<3\sigma$	0.3 ms	$2 \times 10^{-3}$	+35.2 s	$>1$
GW170814	total Earth occultation							
GW170817	total Earth occultation							
GW170818	passage into SAA							
GW170823	passage into SAA							
LV trigger	signal label	trigger start	trigger stop	S/N	$t_{\text{bin}}$	FAR (Hz)	$t - T_0$	FAP
151008	passage into SAA							
151012A	...	...	...	...	...	...	...	...
151116	...	...	...	...	...	...	-	-
161202	<i>trigger a</i>	$T_0 - 23.5$ s	$T_0 - 13.4$ s	$<3\sigma$	16 ms	$5 \times 10^{-3}$	-19.4 s	$>1$
	<i>trigger b</i>	$T_0 + 2.0$ s	$T_0 + 15.3$ s	$<3\sigma$	16 ms	$5 \times 10^{-3}$	+6.1 s	$>1$
161217	...	...	...	...	...	...	...	...
170208	<i>trigger a</i>	$T_0 - 30.4$ s	$T_0 - 16.6$ s	$<3\sigma$	0.3 ms	$2 \times 10^{-3}$	-26.4 s	$>1$
	<i>trigger b</i>	$T_0 + 4.8$ s	$T_0 + 14.2$ s	$<3\sigma$	0.3 ms	$2 \times 10^{-3}$	+8.7 s	$>1$
170219	...	...	...	...	...	...	...	...
170405	<i>trigger a</i>	$T_0 + 16.0$ s	$T_0 + 29.5$ s	$<3\sigma$	16 ms	$5 \times 10^{-3}$	+20.4 s	$>1$
170412*	<i>trigger a</i>	$T_0 - 15.0$ s	$T_0 - 10.1$ s	$<3\sigma$	0.3 ms	$2 \times 10^{-3}$	-14.6 s	$>1$
	<i>trigger b</i>	$T_0 - 0.7$ s	$T_0 + 6.3$ s	$<3\sigma$	0.3 ms	$2 \times 10^{-3}$	-0.20 s	$>1$
	<i>trigger c</i>	$T_0 + 25.8$ s	$T_0 + 34.5$ s	$<3\sigma$	0.3 ms	$2 \times 10^{-3}$	+26.2 s	$>1$
170423	<i>trigger a</i>	$T_0 - 45.6$ s	$T_0 - 31.3$ s	$<3\sigma$	16 ms	$5 \times 10^{-3}$	-45.3 s	$>1$
160616	<i>trigger a</i>	$T_0 - 59.3$ s	$T_0 - 45.1$ s	$<3\sigma$	16 ms	$5 \times 10^{-3}$	-54.4 s	$>1$
	<i>trigger b</i>	$T_0 + 1.3$ s	$T_0 + 15.3$ s	$<3\sigma$	0.3 ms	$2 \times 10^{-3}$	+6.3 s	$>1$
170630	<i>trigger a</i>	$T_0 - 17.6$ s	$T_0 - 2.6$ s	$<3\sigma$	16 ms	$5 \times 10^{-3}$	-13.8 s	$>1$
170705	<i>trigger a</i>	$T_0 - 49.9$ s	$T_0 - 35.0$ s	$<3\sigma$	0.3 ms	$2 \times 10^{-3}$	-46.1 s	$>1$
	<i>trigger b</i>	$T_0 + 49.6$ s	$T_0 + 60.3$ s	$<3\sigma$	16 ms	$5 \times 10^{-3}$	+53.3 s	$>1$
170720	<i>trigger a</i>	$T_0 - 41.6$ s	$T_0 - 26.7$ s	$<3\sigma$	16 ms	$5 \times 10^{-3}$	-37.7 s	$>1$
	<i>trigger b</i>	$T_0 + 35.9$ s	$T_0 + 48.6$ s	$<3\sigma$	16 ms	$5 \times 10^{-3}$	+39.8 s	$>1$

**Note.** GW170104 and LV trigger 170412 (marked with a star) are the only events for which an MCAL onboard data acquisition covers the  $T_0$ . In particular, for GW170104, also a signal is retrieved with a blind search in the corresponding triggered data acquisitions. For each trigger, we report the time duration of the data acquisition (from *trigger start* to *trigger stop*), the signal-to-noise ratio of the event that issued the trigger (S/N), the triggered timescale ( $t_{\text{bin}}$ ), the associated FAR, and the temporal offset from the GW  $T_0$  ( $t - T_0$ ). The time window considered for each search is  $T_0 \pm 50$  s.

**Table 4**  
MCAL UL Fluences for the Accessible GW Events and LV Marginal Triggers

GW Event	MCAL bkg (Hz)	MCAL Configuration	$UL_{\text{MIN}} - UL_{\text{MAX}}$ Model A (erg cm <sup>-2</sup> )	$UL_{\text{MIN}} - UL_{\text{MAX}}$ Model B (erg cm <sup>-2</sup> )	$UL_{\text{MIN}} - UL_{\text{MAX}}$ Model C (erg cm <sup>-2</sup> )
GW150914	553	BASELINE	1.8e-07–3.0e-05	3.9e-08–1.1e-05	2.0e-08–4.1e-06
GW151012	578	BASELINE	1.1e-07–8.5e-06	3.2e-08–3.1e-06	1.7e-08–4.2e-06
GW151226	625	BASELINE	1.1e-07–3.1e-05	3.5e-08–9.1e-06	1.7e-08–4.5e-06
GW170104*	589	MCAL-GW	6.8e-07–4.2e-06	1.9e-07–1.3e-06	1.0e-07–5.9e-07
GW170608	569	MCAL-GW	1.1e-07–5.1e-06	3.1e-08–1.8e-06	1.5e-08–7.1e-07
GW170729	525	MCAL-GW	1.3e-07–2.3e-05	3.1e-08–1.6e-06	1.8e-08–3.3e-06
GW170809	596	MCAL-GW	1.9e-07–2.4e-05	5.4e-08–6.7e-06	2.8e-08–3.5e-06
GW170814			total Earth occultation		
GW170817			total Earth occultation		
GW170818			passage into SAA		
GW170823			passage into SAA		
LV trigger	MCAL bkg (Hz)	MCAL configuration	$UL_{\text{MIN}} - UL_{\text{MAX}}$ model A (erg cm <sup>-2</sup> )	$UL_{\text{MIN}} - UL_{\text{MAX}}$ model B (erg cm <sup>-2</sup> )	$UL_{\text{MIN}} - UL_{\text{MAX}}$ model C (erg cm <sup>-2</sup> )
151008			passage into SAA		
151012A	585	BASELINE	1.1e-07–3.0e-05	3.0e-08–1.4e-05	1.7e-08–4.4e-06
151116	662	BASELINE	1.1e-07–3.2e-05	3.0e-08–9.4e-06	1.7e-08–4.6e-06
161202	593	MCAL-GW	9.9e-08–2.5e-05	2.8e-08–7.7e-06	1.4e-08–3.5e-06
161217	559	MCAL-GW	9.9e-08–2.4e-05	2.8e-08–8.1e-06	1.5e-08–3.3e-06
170208	608	MCAL-GW	9.9e-08–2.4e-05	2.9e-08–7.8e-06	1.5e-08–3.5e-06
170219	614	MCAL-GW	9.9e-08–2.5e-05	2.6e-08–9.2e-06	1.5e-08–3.5e-06
170405	549	MCAL-GW	9.9e-08–2.4e-05	3.1e-08–5.6e-06	1.4e-08–3.4e-06
170412*	569	MCAL-GW	6.8e-07–4.2e-06	1.9e-07–1.6e-06	9.9e-08–5.9e-07
170423	618	MCAL-GW	9.9e-08–2.5e-05	3.1e-08–7.8e-06	1.5e-08–3.5e-06
170616	498	MCAL-GW	9.9e-08–2.2e-05	3.1e-08–8.3e-06	1.4e-08–3.2e-06
170630	605	MCAL-GW	9.9e-08–2.4e-05	2.9e-08–5.9e-06	1.4e-08–3.4e-06
170705	646	MCAL-GW	9.9e-08–2.6e-05	2.7e-08–9.5e-06	1.4e-08–3.7e-06
170720	620	MCAL-GW	9.9e-08–2.5e-05	2.8e-08–1.5e-05	1.5e-08–3.6e-06

**Note.** For each event, the MCAL average background rate in the  $T_0 \pm 50$  s is reported, together with the onboard configuration operative at that time. MCAL ULs are evaluated for a set of different positions inside the 90% credible region, providing a range of values, from  $UL_{\text{MIN}}$  (evaluated on the 0.293 ms timescale) to  $UL_{\text{MAX}}$  (evaluated on the 8,192 ms timescale), depending on the off-axis angle. Fluences are estimated assuming a single power law with photon index  $-1.4$  (model A), a single power law with photon index  $-2.3$  (model B), and a cutoff power-law model with photon index  $-0.62$  and cutoff energy at 185 keV (model C), all evaluated in the 0.4–100 MeV energy range. As GW170104 and LV trigger 170412 are the only events with ongoing MCAL data acquisitions at their  $T_0$ s, their corresponding ULs are  $2\sigma$  UL fluences calculated on 1 s integration (marked with an asterisk). For all the other events, no data are present at the  $T_0$ , and ULs are evaluated on each MCAL timescale by using an independent procedure based on photon counting statistics.

procedure based on photon counting statistics. In order to trigger an onboard data acquisition, an event must release at least  $N$  counts in the detector, where  $N$  is the threshold of a given MCAL logic timescale. In these cases, the UL fluence is represented by the minimum flux capable of producing the  $N$  counts needed to trigger the onboard logic timescale, integrated on the corresponding timescale duration. UL values vary depending on the trigger logic and position inside the

localization region. Each of the seven MCAL timescales has therefore a different set of ( $UL_{\text{min}}$ ;  $UL_{\text{max}}$ ) that are capable of issuing a trigger. As a consequence, for each GW event, we end up with a set of  $7 \times 2$  different UL values. Among these seven ( $UL_{\text{min}}$ ;  $UL_{\text{max}}$ ) pairs, we can select an absolute minimum  $UL_{\text{MIN}}$  and maximum  $UL_{\text{MAX}}$ . In most cases,  $UL_{\text{MIN}}$  is obtained for the shortest-duration timescale, whereas  $UL_{\text{MAX}}$  is obtained for the longest-duration timescale; in Table 4, we report only

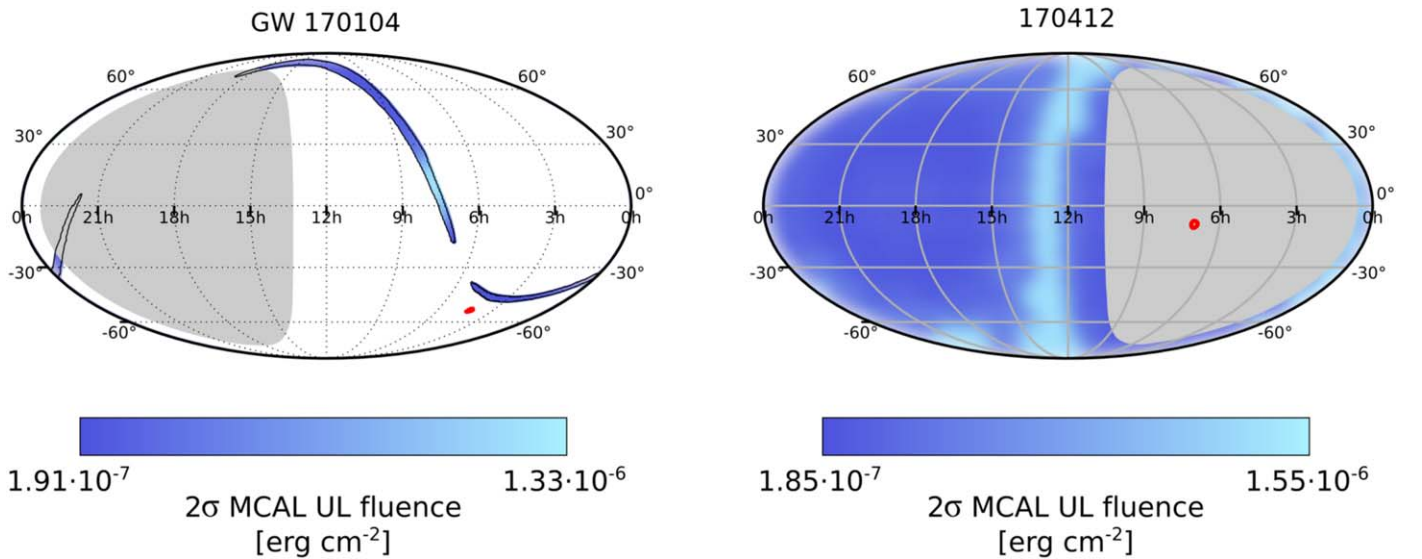


**Figure 2.** Mollweide projection in equatorial coordinates of the AGILE MCAL UL fluences for the only two events, GW170104 and LV trigger 170412, for which MCAL data are available at the  $T_0$ . ULs are calculated as  $2\sigma$  UL fluences, integrated on 1 s. Here, we report only the ULs obtained from spectral model B. The gray region represents the sky zone occulted by the Earth and inaccessible to MCAL. The red dot corresponds to the AGILE boresight.

**Table 5**  
Spectral Models Adopted for the MCAL Fluence ULs Estimate

Model A	Power Law	$\frac{dN}{dE} = KE^\beta$ , with $\beta = -1.4$
Model B	Power Law	$\frac{dN}{dE} = KE^\beta$ , with $\beta = -2.3$
Model C	“Comptonized”	$\frac{dN}{dE} = KE^\beta e^{-\frac{E(2+\beta)}{E_p}}$ , with $\beta = -0.62$ , $E_p = 185$ keV

**Note.** Model A is the power law with photon index  $-1.4$  used to describe the weak GW150914-GBM transient. Model B is a power law with a photon index of  $-2.3$  (typical index of MCAL GRBs). Model C is a cutoff power law used for describing the GRB 170817A.

those two values, for conciseness. An example of one of these sets of ULs is provided in Figure 3 for GW170729, where we report ( $UL_{\min}$ ;  $UL_{\max}$ ) pairs for each trigger timescale. In this case, the lowest fluence UL of the submillisecond logic corresponds to the absolute minimum  $UL_{\min}$ , whereas the highest fluence UL of the 8.192 s logic corresponds to the absolute maximum  $UL_{\max}$ . The values reported in the figure are evaluated for spectral model B.

### 3.3. AGILE GRID Observations

For completeness, we also analyzed GRID data, in order to provide a more complete picture of the AGILE observations of the GWTC-1 events in a broadband energy range. As the GRID is an imaging detector, the portion of the LV localization region accessible to its FOV depends on Earth occultations, as well as on the off-axis angle with respect to each point inside the error region. We considered a time interval of  $\pm 950$  s about each event  $T_0$  and performed an extensive search for transients in the GRID data. No significant electromagnetic emission in the energy range 50 MeV–30 GeV was detected for any of the GW events and of the LV triggers reported in the catalog. We calculated  $3\sigma$  fluxes ULs, evaluated on different time intervals around the  $T_0$ , and estimated on the different portions covered by the GRID FOV at each time. To simulate the fluxes, we

adopted as a spectral model a power law with photon index  $\beta = -1.6$ . Such model was used by AGILE GRID to describe the high-energy (hundreds of MeV) component of GRB 090510 (Giuliani et al. 2010), a well-known candidate to be a BNS merger detected years before the LIGO-Virgo experiment.

#### 3.3.1. AGILE GRID Upper Limits

Table 6 shows GRID fluxes ULs evaluated on different integration times; in particular, we report ULs for  $N$  progressive 100 s integrations from  $T_0 - 950$  s to  $T_0 + 950$  s, and for  $(T_0; T_0 + 5$  s),  $(T_0; T_0 + 10$  s), and  $(T_0; T_0 + 100$  s) integrations, as well as for  $(T_0 - 50$  s;  $T_0 + 50$  s). For each value, the corresponding percentage of accessible contour region is also reported. The GW events with the largest contour regions show the largest number of time intervals with GRID exposure, but cover only fractions of the total error box. On the other hand, GW events with the smallest contour regions fall inside the GRID FOV only at specific times during the satellite spinning but allowing to reach a 100% coverage of the error box. Time intervals with no available ULs are those for which less than 1% of the GW contour region was inside the GRID FOV, due to large off-axis angles reached during the spinning, or due to Earth occultations, or passages into the SAA. In particular, GW170817 is the only event for which no ULs are available at all, during all the time intervals under consideration, as the ongoing Earth occultation finished at about  $T_0 \sim 935$  s. On the other hand, the Earth occultation finished after  $\sim 500$  s in the case of GW170814. An example of a sequence of maps in galactic coordinates showing the GRID 100 s-lasting passes over GW170729 contour region, between interval  $(T_0 - 950$  s;  $T_0 - 850$  s) and interval  $(T_0 + 850$  s;  $T_0 + 950$  s), is shown in Figure 4, with related fluxes ULs in the 30 MeV–50 GeV energy range. In the figure, the FOV changes in time with respect to the contour region, due to the satellite spinning, making the GRID detector cover different fractions of the localization region and provide different UL values with respect to the time interval under analysis.



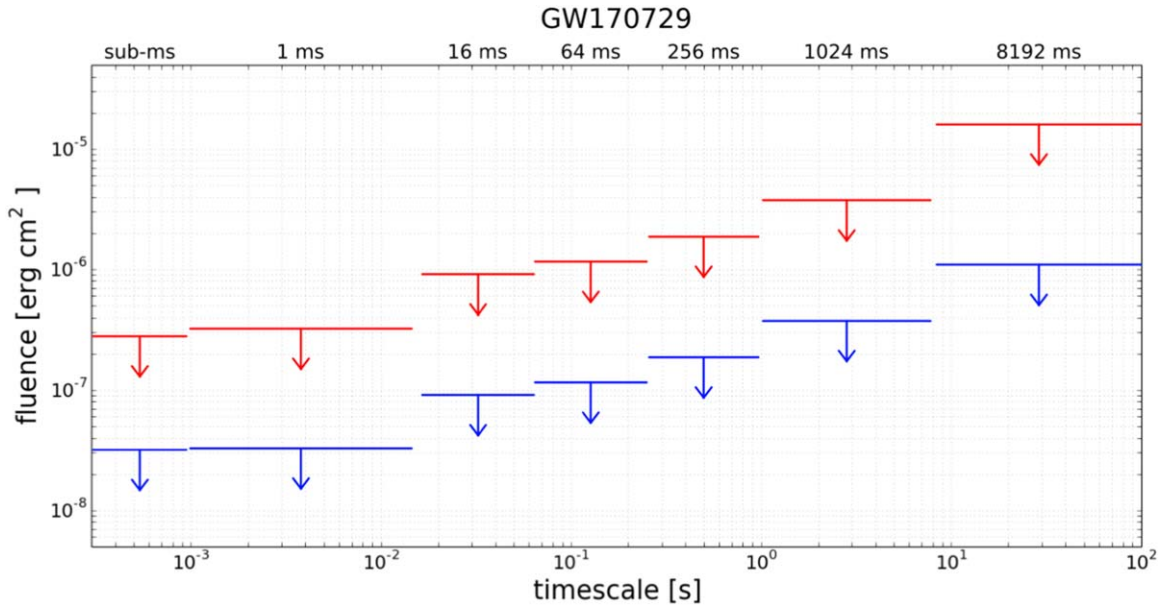


**Figure 3.** MCAL UL fluences for GW170729, integrated on the different onboard trigger logic timescales. Fluence values depend on the different celestial positions considered within the GW credible region, from the most on-axis position  $UL_{\min}$  (blue) to the less on-axis position  $UL_{\max}$  (red). The lowest fluence in the submillisecond timescale corresponds to the absolute minimum  $UL_{\min}$ , whereas the highest fluence in the 8.192 s timescale corresponds to the absolute maximum  $UL_{\max}$ . Here, we report only the values obtained from spectral model B.

#### 4. Discussion

The joint detection of BNS (GW170817 and GRB 170817A) provided the first direct evidence of BNS mergers as short GRBs progenitors. BNS and NSBH were already expected to be the most likely candidate sources of short GRBs, due to strong support by observational indirect evidence (e.g., host galaxies, environmental densities), as well as by theoretical models (e.g., modeling of magnetic fields, jet production) (Rosswog 2005; Troja et al. 2008; Rezzolla et al. 2011; Fong et al. 2015).

On the other hand, BBHs are not expected to produce an associated EM emission. However, some studies point out that, depending on the geometry, mass, and rotation involved in the system, BBH mergers may exhibit some EM emission associated with the GW event; a short “GRB-like” EM emission may arise from an ephemeral accretion on the BH resulting from the merger, seeded circumbinary disks or common envelopes that could constitute these systems (Loeb 2016; Perna et al. 2016; Woosley 2016).

Due to the larger masses and higher gravitational energy released, BBHs represent the most detected events by the LV experiments. During the O1 and O2 runs, the EM follow-up community delivered a large number of GCNs concerning the search for counterparts to these events. Connaughton et al. 2016 reported the Fermi GBM detection of a weak gamma-ray signal lasting  $\sim 1$  s, similar to a low-fluence short GRB, observed about 0.4 s after the GW150914, whereas Verrecchia et al. (2017b) reported the detection of a weak 0.32 ms pulse occurring immediately before the LV  $T_0$ . Neither of these detections was confirmed by other space missions and observatories, which prevented them from being validated as true astrophysical events. In all other cases, no associated EM emission was detected and UL fluences were provided in different energy ranges.

For what concerns GRB 170817A, the associated GW event localization region was not accessible to AGILE at the  $T_0$ , due

to a complete Earth occultation (Verrecchia et al. 2017a). Due to the spinning, which makes the satellite scan  $\sim 80\%$  of the accessible sky every 7 minutes, AGILE collected useful data after the occultation: the GRID detector provided the earliest exposure of the GW event credible region at  $T_0 + 935$  s, consisting in one of the closest in time measurements of the event localization region obtained by space satellites. Such observations allowed to put useful constraints on precursor and delayed emissions of the BNS coalescence, leading to the exclusion of a high-energy emitting magnetar-like object with a high  $\sim 10^{15}$  G magnetic field, as well as of models involving gamma-ray luminosities  $L \sim 10^{45}$  erg  $s^{-1}$  at 1000 s after the coalescence (Duncan & Thompson 1992; Usov 1992; Thompson 1994; Spruit 1999; Zhang & Mészáros 2001).

##### 4.1. MCAL Potential Detection of BBH-associated EM Emission

The 7 + 13 BBHs that produced the GW events accessible to AGILE at the  $T_0$  exhibit different distances, redshifts, and radiated energies, which are reported in Table 2. The closest and less energetic BBH event is GW170608, occurring at  $d_L \sim 320$  Mpc ( $z = 0.07$ ) and releasing  $E_{\text{rad}} = 0.9M_{\odot}c^2 = 1.7 \times 10^{57}$  erg, for which the minimum MCAL UL detectable fluence is  $F_{\text{UL}} = 1.45 \times 10^{-8}$  erg  $\text{cm}^{-2}$  (for model C). Such a value would correspond to a UL isotropic equivalent energy at that distance equal to  $E_{\text{iso}}^{\text{UL}} = F_{\text{UL}} \frac{4\pi d_L^2}{(1+z)} = 1.66 \times 10^{47}$  erg. On the other hand, the farthest and most energetic BBH event is GW170729, occurring at  $d_L \sim 2750$  Mpc ( $z = 0.58$ ) and releasing  $E_{\text{rad}} = 4.8M_{\odot}c^2 = 8.6 \times 10^{57}$  erg. In this case, the minimum MCAL UL fluence is equal to  $F_{\text{UL}} = 1.77 \times 10^{-8}$  erg  $\text{cm}^{-2}$  (for model C) and the related UL isotropic equivalent energy is  $E_{\text{iso}}^{\text{UL}} = F_{\text{UL}} \frac{4\pi d_L^2}{(1+z)} = 1.08 \times 10^{49}$  erg. If using model A, which produces the larger UL values, the corresponding isotropic energies for GW170608 and GW170729 would be  $E_{\text{iso}}^{\text{UL}} = 1.26 \times 10^{48}$  erg and  $E_{\text{iso}}^{\text{UL}} = 7.64 \times 10^{49}$  erg, respectively. All

**Table 6**  
AGILE GRID fluxes ULs

	<b>GW150914</b>		<b>GW151012</b>		<b>GW151226</b>		<b>GW170104</b>	
<b>int. time</b> [s]	$UL_{\min}-UL_{\max}$ [erg cm <sup>-2</sup> s <sup>-1</sup> ]	<b>a.r.</b>	$UL_{\min}-UL_{\max}$ [erg cm <sup>-2</sup> s <sup>-1</sup> ]	<b>a.r.</b>	$UL_{\min}-UL_{\max}$ [erg cm <sup>-2</sup> s <sup>-1</sup> ]	<b>a.r.</b>	$UL_{\min}-UL_{\max}$ [erg cm <sup>-2</sup> s <sup>-1</sup> ]	<b>a.r.</b>
$T_0-950; T_0-850$	5.7e-08–1.2e-07	61%	1.3e-07–4.0e-06	9%	2.8e-07–3.3e-06	1%	5.6e-08–1.4e-06	68%
$T_0-850; T_0-750$	...	0%	2.9e-08–2.2e-06	45%	...	0%	2.9e-08–1.5e-06	18%
$T_0-750; T_0-650$	...	0%	3.0e-08–4.0e-07	78%	...	0%	1.2e-07–3.7e-06	25%
$T_0-650; T_0-550$	5.2e-08–7.4e-08	72%	3.1e-08–1.1e-06	62%	...	0%	3.5e-08–1.3e-06	67%
$T_0-550; T_0-450$	3.5e-08–5.6e-08	74%	2.1e-07–7.3e-06	13%	...	0%	2.9e-08–1.3e-07	78%
$T_0-450; T_0-350$	2.5e-06–9.9e-06	26%	4.0e-08–2.9e-06	28%	...	0%	5.1e-08–1.7e-06	74%
$T_0-350; T_0-250$	...	0%	3.0e-08–1.1e-06	74%	5.1e-08–1.5e-06	19%	2.9e-08–2.0e-06	20%
$T_0-250; T_0-150$	1.1e-07–2.7e-07	82%	3.0e-08–4.0e-07	75%	4.4e-08–3.9e-06	5%	8.0e-08–5.6e-06	16%
$T_0-150; T_0-50$	3.0e-08–3.6e-08	84%	3.8e-08–2.2e-06	47%	3.5e-08–3.3e-07	5%	4.0e-08–1.6e-06	55%
$T_0-50; T_0+50$	1.9e-07–1.4e-06	86%	1.3e-07–3.6e-06	14%	4.0e-08–1.5e-06	26%	2.9e-08–3.0e-07	58%
$T_0; T_0+5$	...	0%	3.2e-06–9.9e-06	1%	6.4e-07–5.6e-06	12%	5.4e-07–1.5e-06	51%
$T_0; T_0+10$	...	0%	1.6e-06–9.9e-06	2%	3.3e-07–4.0e-06	14%	2.7e-07–7.9e-07	51%
$T_0; T_0+100$	...	0%	4.1e-08–3.1e-06	26%	3.9e-08–7.7e-07	34%	3.1e-08–5.1e-07	51%
$T_0+50; T_0+150$	...	0%	2.9e-08–2.2e-06	43%	3.0e-08–4.0e-07	37%	5.4e-08–2.4e-06	48%
$T_0+150; T_0+250$	...	0%	3.0e-08–4.9e-07	78%	4.4e-08–7.0e-07	32%	3.0e-08–2.8e-07	14%
$T_0+250; T_0+350$	...	0%	3.1e-08–8.8e-07	66%	7.4e-08–6.4e-06	6%	6.1e-08–2.5e-07	14%
$T_0+350; T_0+450$	...	0%	8.7e-08–4.5e-06	16%	7.1e-08–3.2e-06	4%	4.9e-08–6.2e-07	31%
$T_0+450; T_0+550$	...	0%	4.1e-08–2.8e-06	22%	3.3e-08–2.2e-06	23%	3.0e-08–2.1e-07	31%
$T_0+550; T_0+650$	...	0%	3.0e-08–1.4e-06	64%	3.3e-08–6.7e-07	40%	5.6e-08–2.4e-06	29%
$T_0+650; T_0+750$	...	0%	3.0e-08–2.9e-07	68%	3.8e-08–4.6e-07	35%	3.2e-08–3.0e-07	14%
$T_0+750; T_0+850$	...	0%	3.6e-08–1.9e-06	48%	4.1e-08–3.3e-06	18%	4.9e-08–2.0e-07	15%
$T_0+850; T_0+950$	...	0%	1.4e-07–4.6e-06	12%	9.4e-08–1.3e-06	16%	6.1e-08–7.3e-07	26%
	<b>GW170608</b>		<b>GW170729</b>		<b>GW170809</b>		<b>GW170814</b>	
<b>int. time</b> [s]	$UL_{\min}-UL_{\max}$ [erg cm <sup>-2</sup> s <sup>-1</sup> ]	<b>a.r.</b>	$UL_{\min}-UL_{\max}$ [erg cm <sup>-2</sup> s <sup>-1</sup> ]	<b>a.r.</b>	$UL_{\min}-UL_{\max}$ [erg cm <sup>-2</sup> s <sup>-1</sup> ]	<b>a.r.</b>	$UL_{\min}-UL_{\max}$ [erg cm <sup>-2</sup> s <sup>-1</sup> ]	<b>a.r.</b>
$T_0-950; T_0-850$	2.0e-07–5.8e-07	14%	1.1e-07–2.7e-06	5%	6.2e-07–9.8e-06	10%	...	0%
$T_0-850; T_0-750$	4.7e-08–6.5e-08	14%	4.6e-08–1.4e-06	11%	6.1e-08–3.9e-07	25%	...	0%
$T_0-750; T_0-650$	7.7e-07–9.1e-06	13%	3.3e-08–1.3e-06	18%	2.8e-07–3.3e-06	15%	...	0%
$T_0-650; T_0-550$	...	0%	3.3e-08–4.1e-06	14%	...	0%	...	0%
$T_0-550; T_0-450$	1.6e-07–4.1e-07	17%	4.4e-08–3.6e-06	7%	8.5e-08–1.8e-06	64%	...	0%
$T_0-450; T_0-350$	4.6e-08–5.8e-08	17%	3.8e-08–1.3e-06	23%	3.9e-08–2.4e-07	76%	...	0%
$T_0-350; T_0-250$	9.5e-07–9.6e-06	10%	2.9e-08–4.2e-07	32%	3.5e-07–4.4e-06	33%	...	0%
$T_0-250; v-150$	...	0%	5.0e-08–1.3e-06	26%	...	0%	...	0%
$T_0-150; T_0-50$	1.4e-07–4.5e-07	22%	3.5e-08–2.0e-06	4%	6.0e-08–8.6e-07	99%	...	0%
$T_0-50; T_0+50$	4.7e-08–6.5e-08	23%	7.1e-08–3.6e-06	23%	3.6e-08–2.2e-07	99%	...	0%
$T_0; T_0+5$	7.5e-07–1.2e-06	22%	1.3e-06–4.6e-06	9%	6.0e-07–3.2e-06	95%	...	0%
$T_0; T_0+10$	3.8e-07–6.3e-07	22%	5.9e-07–3.8e-06	10%	3.0e-07–1.8e-06	95%	...	0%
$T_0; T_0+100$	8.9e-08–2.8e-07	23%	3.8e-08–8.7e-07	45%	6.7e-08–1.7e-06	95%	...	0%

**Table 6**  
(Continued)

GW150914			GW151012			GW151226			GW170104		
int. time [s]	$UL_{\min}-UL_{\max}$ [erg cm <sup>-2</sup> s <sup>-1</sup> ]	a.r.	$UL_{\min}-UL_{\max}$ [erg cm <sup>-2</sup> s <sup>-1</sup> ]	a.r.	$UL_{\min}-UL_{\max}$ [erg cm <sup>-2</sup> s <sup>-1</sup> ]	a.r.	$UL_{\min}-UL_{\max}$ [erg cm <sup>-2</sup> s <sup>-1</sup> ]	a.r.			
$T_0+50; T_0+150$	8.4e-07–9.8e-06	11%	3.2e-08–3.3e-07	50%	5.6e-07–5.7e-06	31%	...	0%			
$T_0+150; T_0+250$	...	0%	3.4e-08–1.1e-06	49%	...	0%	...	0%			
$T_0+250; T_0+350$	1.1e-07–4.1e-07	32%	2.2e-07–7.3e-06	9%	5.3e-08–5.6e-07	99%	...	0%			
$T_0+350; T_0+450$	4.7e-08–9.6e-08	34%	2.3e-07–4.0e-06	11%	3.6e-08–2.4e-07	99%	...	0%			
$T_0+450; T_0+550$	8.4e-07–9.7e-06	11%	3.6e-08–1.7e-06	60%	9.9e-07–7.4e-06	20%	6.7e-08–1.1e-07	100%			
$T_0+550; T_0+650$	1.8e-07–1.8e-06	51%	3.0e-08–3.3e-07	68%	...	0%	3.7e-08–4.2e-08	100%			
$T_0+650; T_0+750$	7.5e-08–2.2e-07	100%	7.1e-08–1.7e-06	46%	4.7e-08–3.8e-07	99%	2.2e-06–1.0e-05	58%			
$T_0+750; T_0+850$	5.1e-08–1.5e-06	66%	6.1e-08–5.3e-06	2%	3.8e-08–2.6e-07	99%	...	0%			
$T_0+850; T_0+950$	2.5e-06–1.0e-05	3%	5.1e-08–3.0e-06	36%	1.5e-06–8.9e-06	12%	1.5e-07–3.9e-07	100%			
GW170817			GW170818			GW170823					
int. time [s]	$UL_{\min}-UL_{\max}$ [erg cm <sup>-2</sup> s <sup>-1</sup> ]	a.r.	$UL_{\min}-UL_{\max}$ [erg cm <sup>-2</sup> s <sup>-1</sup> ]	a.r.	$UL_{\min}-UL_{\max}$ [erg cm <sup>-2</sup> s <sup>-1</sup> ]	a.r.					
$T_0-950; T_0-850$	...	0%	...	0%	2.9e-08–8.1e-08	59%					
$T_0-850; T_0-750$	...	0%	...	0%	5.6e-08–2.8e-06	35%					
$T_0-750; T_0-650$	...	0%	6.9e-08–1.3e-07	100%	6.3e-08–4.5e-07	0%					
$T_0-650; T_0-550$	...	0%	2.7e-07–3.9e-07	100%	9.3e-08–3.7e-06	27%					
$T_0-550; T_0-450$	...	0%	...	0%	2.9e-08–1.5e-07	52%					
$T_0-450; T_0-350$	...	0%	...	0%	3.4e-08–2.4e-07	50%					
$T_0-350; T_0-250$	...	0%	5.4e-07–1.3e-06	100%	8.0e-07–7.3e-06	10%					
$T_0-250; T_0-150$	...	0%	...	0%	...	0%					
$T_0-150; T_0-50$	...	0%	...	0%	...	0%					
$T_0-50; T_0+50$	...	0%	...	0%	...	0%					
$T_0; T_0+5$	...	0%	...	0%	...	0%					
$T_0; T_0+10$	...	0%	...	0%	...	0%					
$T_0; T_0+100$	...	0%	...	0%	...	0%					
$T_0+50; T_0+150$	...	0%	...	0%	...	0%					
$T_0+150; T_0+250$	...	0%	...	0%	...	0%					
$T_0+250; T_0+350$	...	0%	...	0%	...	0%					
$T_0+350; T_0+450$	...	0%	...	0%	6.6e-08–5.8e-07	28%					
$T_0+450; T_0+550$	...	0%	...	0%	4.8e-08–1.3e-06	22%					
$T_0+550; T_0+650$	...	0%	2.0e-07–3.0e-07	100%	7.4e-08–3.3e-06	11%					
$T_0+650; T_0+750$	...	0%	...	0%	3.0e-08–9.9e-07	32%					
$T_0+750; T_0+850$	...	0%	...	0%	2.9e-08–2.0e-07	45%					
$T_0+850; T_0+950$	...	0%	3.6e-07–8.0e-07	100%	3.6e-08–1.1e-06	26%					

**Note.** GRID ULs are estimated in the 30 MeV–50 GeV energy range. AGILE GRID fluxes ULs obtained in a time frame of  $\pm 950$ s about each of the 11 GW  $T_0$ s, at steps of 5, 10, and 100s, with the corresponding fraction of accessible region (a.r.) at each time interval.

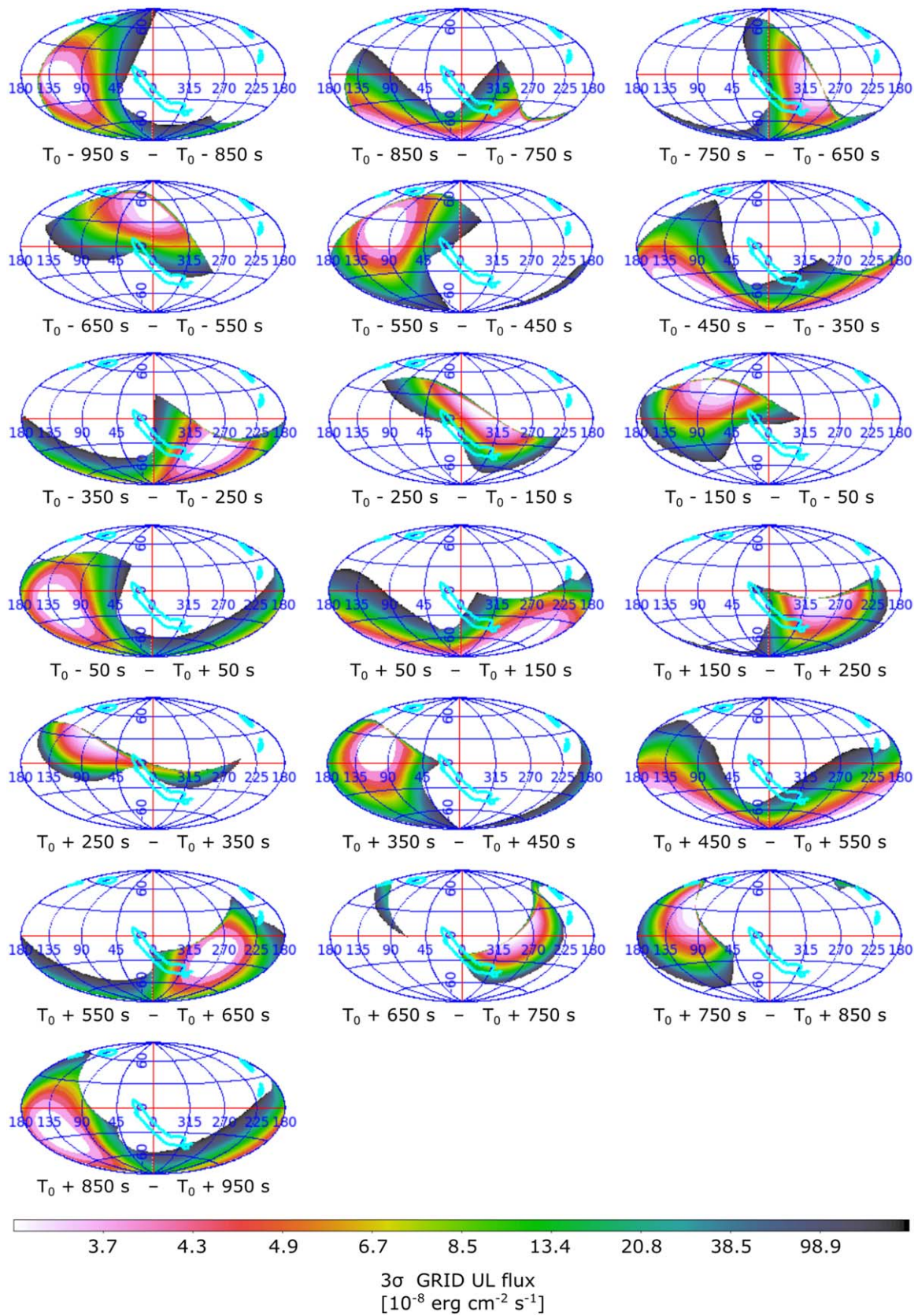


**Figure 4.** A sequence of GRID 100 s-lasting passes over the GW170729 contour region (cyan) and corresponding flux UL values, evaluated in a time frame from  $T_0 - 950$  s to  $T_0 + 950$  s, in the 30 MeV–50 GeV energy range. The FOV and the related UL values change in time with respect to the contour region, due to the satellite spinning about its Sun-pointing axis. As a consequence, the fractions of localization region covered by the GRID change in time, as well as the fluxes ULs.

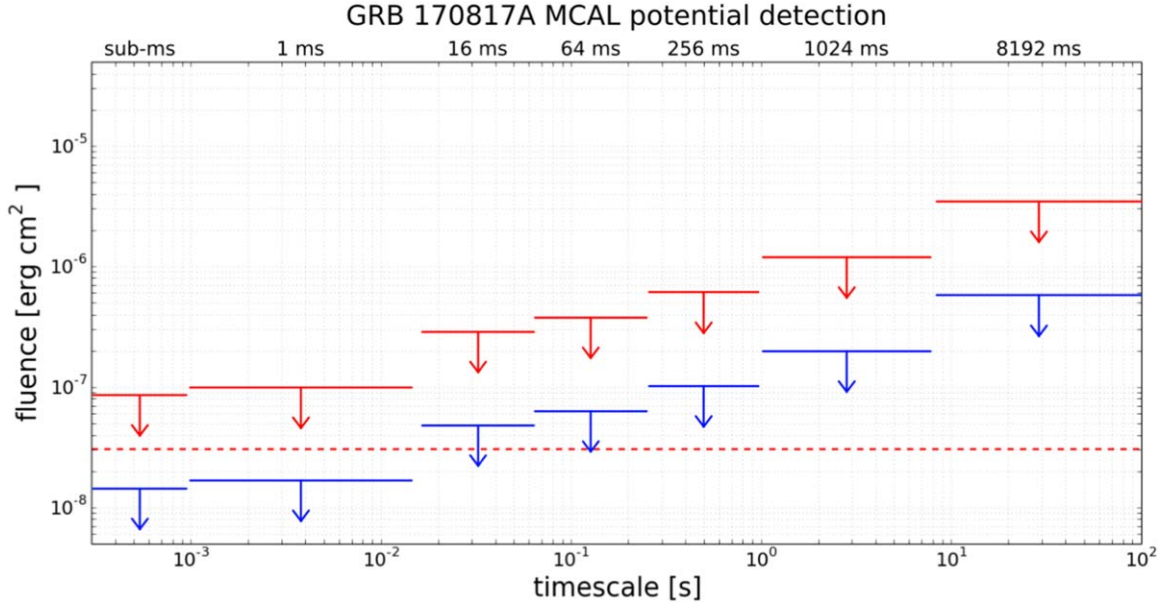


**Figure 5.** MCAL UL fluences in the seven onboard logic timescales, for a typical 570 Hz background rate, in the “MCAL-GW” configuration, evaluated on the 400 keV–100 MeV. For each timescale, UL values range from a  $UL_{\min}$  (most on-axis configuration, in blue) to  $UL_{\max}$  (less on-axis configuration, in red). The dashed red line corresponds to the reconstructed GRB 170817A fluence in the same energy range, expected if considering the same spectral model adopted for Fermi GBM data. It can be seen that, under favorable conditions of off-axis angle, a weak soft-spectrum event such as GRB 170817A could have been, in principle, detected by the AGILE MCAL, at least in the submillisecond and in the 1 ms trigger logic timescales.

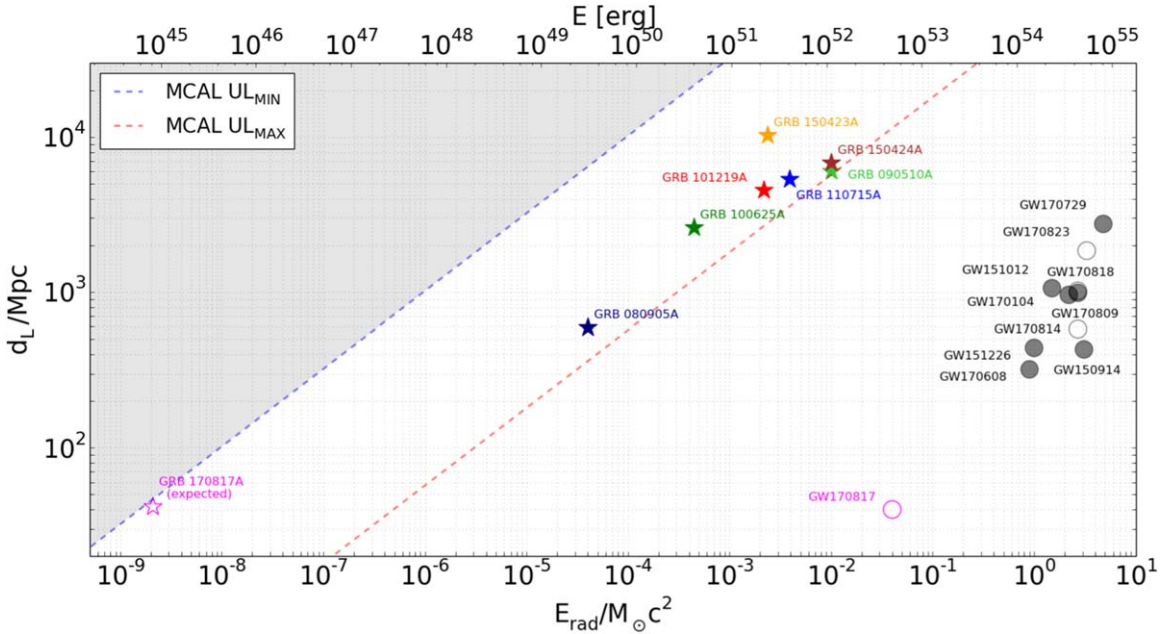


**Figure 6.** Short GRBs (stars) with related  $E_{\text{iso}}$  (in the MCAL energy range) and GW events (circles) with related radiated energy  $E_{\text{rad}}$ , released in gravitational waves. Dashed lines represent the absolute minimum MCAL  $UL_{\min}$  (blue) and the absolute maximum MCAL  $UL_{\max}$  (red), obtained from model C (the “comptonized” model). The gray region indicates the area in the parameter space where events are not detectable by MCAL.

these values are rather smaller than the typical  $E_{\text{iso}}$  released by GRBs detected by MCAL, whose average value is on the order of  $\sim 10^{51}$ – $10^{52}$  erg. However, the only EM emission associated with a GW event detected so far, that is, short GRB 170817A associated with GW170817, exhibited a softer spectrum with respect to typical short hard GRBs and a smaller isotropic energy  $E_{\text{iso}} = 5.6 \times 10^{46}$  erg, as reconstructed by Fermi GBM (Goldstein et al. 2017), assuming a structured jet profile seen from a wide viewing angle.

#### 4.2. MCAL Potential Detection of Fermi GW150914-GBM

At the GW150914  $T_0$ , a large fraction (80%) of the event credible region was accessible to the AGILE satellite, but no significant EM emissions have been detected. It is therefore interesting to compare the MCAL fluence ULs obtained for GW150914 with the fluence of the hard X-ray weak transient GW150914-GBM detected by Fermi GBM, about 0.4 s after the GW event.

Connaughton et al. (2016) reported a best fit for GW150914-GBM, obtained with a power law with photon index  $-1.4$ , in the  $1\text{--}1000$  keV energy range, resulting in a fluence of  $\sim 2.4 \times 10^{-7}$  erg cm $^{-2}$ . The same model, in the MCAL energy range, would produce a fluence of  $\sim 4.0 \times 10^{-6}$  erg cm $^{-2}$ . Table 4 reports the MCAL absolute minimum and maximum fluence ULs, obtained inside the GW150914 credible region, among the seven trigger logic timescales; these values range from  $UL_{\text{MIN}} = 1.8 \times 10^{-7}$  erg cm $^{-2}$  to  $UL_{\text{MAX}} = 3.0 \times 10^{-5}$  erg cm $^{-2}$ . On the other hand, if we only focus on the GW150914-GBM best localization provided by Fermi GBM (R.A. =  $75^\circ$ , decl. =  $-73^\circ$ ), we can reconstruct the fluence ULs corresponding to that specific sky position, which turns out to range between  $UL_{\text{min}} = 6.9 \times 10^{-7}$  erg cm $^{-2}$  (for the submillisecond timescale) and  $UL_{\text{max}} = 1.0 \times 10^{-5}$  erg cm $^{-2}$  (for the 8.192 s timescale). This position was fully accessible to AGILE and  $48^\circ$  off-axis with respect to the satellite boresight.

We notice that, in both cases, the MCAL minimum detectable fluence is lower than the fluence expected from GW150914-GBM in the  $0.4\text{--}100$  MeV energy range. As a consequence, GW150914-GBM should have, in principle, triggered the AGILE MCAL, at least in the shortest-duration timescale trigger logics. The fact that MCAL did not detect this transient suggests the existence of a spectral cutoff below  $E_p \leq 7$  MeV, which could justify a fainter fluence in the MCAL hard energy range. Another possibility is that the GW150914-GBM position was inside the 20% fraction of credible region inaccessible to AGILE at the  $T_0$ .

#### 4.3. MCAL Potential Detection of GRB 170817A

MCAL has detected so far a large fraction of short-duration, hard-spectrum GRBs (Ursi et al. 2021) and it is interesting to investigate whether a weak, soft-spectrum burst as GRB 170817A would have been potentially detected by MCAL, if its contour region was not occulted by the Earth at the  $T_0$ . Taking into consideration the ‘‘comptonized model’’ (model C) suggested by Goldstein et al. (2017) to analyze Fermi GBM data and to fit the main 0.5 s-lasting peak of GRB 170817A in the  $10\text{--}1000$  keV energy range, we calculated the corresponding expected fluence in the MCAL band, which turned out to be equal to  $F_{\text{MCAL}}^{\text{exp}} = 3.07 \times 10^{-8}$  erg cm $^{-2}$ . It must be noticed that GRB 170817A exhibits a softer spectrum with respect to other typical short hard GRBs, showing a sharp cutoff above  $\sim 200$  keV. As a consequence, most of the spectrum detectable by MCAL comes from the 400-1000 keV band, with no significant component arising extending the integration up to 100 MeV. The obtained fluence corresponds to about  $\sim 11\%$  of the fluence detected by Fermi GBM, and it translates into an isotropic equivalent energy of  $E_{\text{iso}}^{\text{exp}} = 5.8 \times 10^{45}$  erg, about one order of magnitude lower than that obtained from Fermi data.  $F_{\text{MCAL}}^{\text{exp}}$  is on the order of the smallest ULs provided by MCAL for the BBH GW events. In Figure 5, the MCAL ( $UL_{\text{min}}$ ;  $UL_{\text{max}}$ ) pair evaluated on the seven different MCAL onboard trigger logic timescales are reported, estimated in the 400 keV–100 MeV energy range, for a typical background rate of 570 Hz, and in the ‘‘MCAL-GW’’ configuration. The red dashed line corresponds to the GRB 170817A expected fluence  $F_{\text{MCAL}}^{\text{exp}}$ . As a consequence, in the best conditions of angular configuration, with a standard  $\sim 570$  Hz background rate, and running the ‘‘MCAL-GW’’ configuration, a weak soft-spectrum event such as GRB 170817A would have been triggered by the AGILE MCAL.

Figure 6 shows an energy-distance plot with LV GW events and MCAL GRBs. In particular, it reports all GW events (circles) detected by LV during O1 and O2, with associated energy emitted in gravitational waves  $E_{\text{rad}}$  and luminosity distance  $d_L$ . A sample of short GRBs (stars) detected by MCAL is also reported in the figure, with the related isotropic equivalent energy  $E_{\text{iso}}$  evaluated above 400 keV. In the plot, filled markers represent events that were accessible to AGILE; in particular, filled circles represent GW events whose contour region was accessible, or partially accessible, to AGILE MCAL, (i.e., events for which a potential EM emission could be detected), whereas filled stars represent GRBs detected by MCAL. On the other hand, hollow markers identify events that were not accessible to AGILE, that is GW events whose contour region was not observable by the satellite at  $T_0$ , as well as the GRB 170817A not detected by MCAL. For this event, we report the expected  $E_{\text{iso}}$ , released in the MCAL energy range. In the plot, the gray shaded area corresponds to the region in the parameter space where events would not be triggered by MCAL. Dashed lines represent the absolute minimum MCAL fluence UL obtained for the less conservative configuration ( $UL_{\text{MIN}}$ , in blue) and the absolute maximum MCAL fluence UL obtained for the less sensitive configuration ( $UL_{\text{MAX}}$ , in red), respectively, evaluated for model C. We point out that the expected emission of GRB 170817A above 400 keV lies inside the MCAL detectability region, and that, in a condition of favorable off-axis angle and background rate, the event would have been detected by MCAL, at least in the submillisecond and in the 1 ms trigger logic timescales.

## 5. Conclusions

We carried out a systematic search for possible electromagnetic counterparts of the GW events and marginal triggers reported in the LIGO-Virgo GWTC-1 catalog. The analysis of AGILE MCAL and AGILE GRID data in a time interval of  $T_0 \pm 50$  s and  $T_0 \pm 950$  s about each event, respectively, led to the identification of no significant electromagnetic emission associated with the LV events. The only exception is represented by the faint 0.32 ms lasting signal detected nearby GW170104 and already discussed in Verrecchia et al. (2017b).

We report detailed AGILE upper limit fluxes and fluences, evaluated on the portions of LV 90% credible region accessible to the satellite at each time interval under consideration. MCAL upper limit fluences have been calculated in the 400 keV–100 MeV energy range, by considering the detector background rate, the onboard trigger configuration, the off-axis angle, the energy range, and adopting three different spectral models. UL fluences have been evaluated on different integration times, depending on whether a data acquisition was ongoing at the  $T_0$ , or not. For each GW event and LV trigger, we reported the corresponding MCAL fluence ULs, from the minimum  $UL_{\text{MIN}}^{\text{MCAL}}$  value achieved in the shortest-duration timescale, with the less conservative onboard configuration and best sensitivity, to the maximum  $UL_{\text{MAX}}^{\text{MCAL}}$  achieved in the longest-duration timescale, with the most conservative configuration. Similarly, GRID flux ULs have been evaluated on different integration times around the  $T_0$ , in the 30 MeV–50 GeV energy range, and adopting a power law with spectral index  $\beta = -1.6$ . For each GW event, we reported the corresponding  $3\sigma$  UL range, from  $UL_{\text{min}}^{\text{GRID}}$  to  $UL_{\text{max}}^{\text{GRID}}$ .





Finally, we evaluated whether a soft-spectrum burst such as GRB 170817A would have triggered the AGILE MCAL, if its

localization region was not occulted by the Earth at the  $T_0$ . We calculated the expected GRB 170817A fluence in the MCAL energy range, adopting the same “comptonized” spectral model used by Goldstein et al. (2017) to fit Fermi GBM data. From this analysis, we conclude that, in favorable conditions of on-axis angle configuration and for a typical MCAL background rate, GRB 170817A could have triggered the AGILE MCAL, at least in the submillisecond and in the 1 ms trigger logic timescales.

This work represents a comprehensive catalog of the AGILE observations of LIGO-Virgo events, after a detailed and systematic offline reanalysis. Similar work will be carried out once the complete second GWTC-2 catalog covering the whole O3 is released, including GW events of particular interest, as the first-ever detected NSBH events.

AGILE is a mission of the Italian Space Agency (ASI), with coparticipation of INAF (Istituto Nazionale di Astrofisica) and INFN (Istituto Nazionale di Fisica Nucleare). This work was carried out in the frame of the ASI-INAF agreement I/028/12/5.

### ORCID iDs

A. Ursi  <https://orcid.org/0000-0002-7253-9721>  
 F. Verrecchia  <https://orcid.org/0000-0003-3455-5082>  
 G. Piano  <https://orcid.org/0000-0002-9332-5319>  
 C. Casentini  <https://orcid.org/0000-0001-8100-0579>  
 M. Tavani  <https://orcid.org/0000-0003-2893-1459>  
 A. Bulgarelli  <https://orcid.org/0000-0001-6347-0649>  
 M. Cardillo  <https://orcid.org/0000-0001-8877-3996>  
 F. Longo  <https://orcid.org/0000-0003-2501-2270>  
 F. Lucarelli  <https://orcid.org/0000-0002-6311-764X>  
 A. Morselli  <https://orcid.org/0000-0002-7704-9553>  
 N. Parmiggiani  <https://orcid.org/0000-0002-4535-5329>  
 M. Pilia  <https://orcid.org/0000-0001-7397-8091>  
 C. Pittori  <https://orcid.org/0000-0001-6661-9779>

### References

Abbott, B. P., Abbott, R., Abbott, T. D., et al. 2016a, *PhRvL*, **116**, 061102  
 Abbott, B. P., Abbott, R., Abbott, T. D., et al. 2016b, *PhRvD*, **93**, 122003  
 Abbott, B. P., Abbott, R., Abbott, T. D., et al. 2016c, *PhRvX*, **6**, 041015  
 Abbott, B. P., Abbott, R., Abbott, T. D., et al. 2016d, *PhRvL*, **116**, 241103  
 Abbott, B. P., Abbott, R., Abbott, T. D., et al. 2017a, *PhRvL*, **118**, 221101  
 Abbott, B. P., Abbott, R., Abbott, T. D., et al. 2017b, *ApJL*, **851**, L35

Abbott, B. P., Abbott, R., Abbott, T. D., et al. 2017c, *PhRvL*, **119**, 141101  
 Abbott, B. P., Abbott, R., Abbott, T. D., et al. 2017d, *PhRvL*, **119**, 161101  
 Abbott, B. P., Abbott, R., Abbott, T. D., et al. 2017e, *ApJL*, **848**, L13  
 Abbott, B. P., Abbott, R., Abbott, T. D., et al. 2017f, *ApJL*, **848**, L12  
 Abbott, B. P., Abbott, R., Abbott, T. D., et al. 2019, *PhRvX*, **9**, 031040  
 Abbott, R., Abbott, T. D., Abraham, S., et al. 2021, *PhRvX*, **11**, 021053  
 Acernese, F., Agathos, M., Agatsuma, K., et al. 2015, *CQGra*, **32**, 024001  
 Barbiellini, G., Fedel, G., Liello, F., et al. 2002, *NIMPA*, **490**, 146  
 Bulgarelli, A. 2019a, *ExA*, **48**, 199  
 Bulgarelli, A. 2019b, *RLSFN*, **30**, 207  
 Connaughton, V., Burns, E., Goldstein, A., et al. 2016, *ApJL*, **826**, L6  
 Del Monte, E., Barbiellini, G., Donnarumma, I., et al. 2011, *A&A*, **535**, A120  
 Del Monte, E., Costa, E., Donnarumma, I., et al. 2009, in AIP Conf. Proc. 1133, *GAMMA-RAY BURST: Sixth Huntsville Symposium* (Melville, NY: AIP), 12  
 Duncan, R. C., & Thompson, C. 1992, *ApJL*, **392**, L9  
 Fong, W., Berger, E., Margutti, R., & Zauderer, B. A. 2015, *ApJ*, **815**, 102  
 Galli, M., Marisaldi, M., Fuschino, F., et al. 2013, *A&A*, **553**, A33  
 Giuliani, A., Fuschino, F., Vianello, G., et al. 2010, *ApJL*, **708**, L84  
 Giuliani, A., Mereghetti, S., Fornari, F., et al. 2008, *A&A*, **491**, L25  
 Goldstein, A., Veres, P., Burns, E., et al. 2017, *ApJL*, **848**, L14  
 Labanti, C., Marisaldi, M., Fuschino, F., et al. 2009, *NIMPA*, **598**, 470  
 LIGO Scientific Collaboration, Aasi, J., Abbott, B. P., et al. 2015, *CQGra*, **32**, 074001  
 Loeb, A. 2016, *ApJL*, **819**, L21  
 Maiorana, C., Marisaldi, M., Lindanger, A., et al. 2020, *JGRD*, **125**, e31986  
 Marisaldi, M., Fuschino, F., Labanti, C., et al. 2010, *JGRA*, **115**, A00E13  
 Marisaldi, M., Fuschino, F., Tavani, M., et al. 2014, *JGRA*, **119**, 1337  
 Marisaldi, M., Labanti, C., Fuschino, F., et al. 2008, in AIP Conf. Proc. 1000, *GAMMA-RAY BURSTS 2007* (Melville, NY: AIP), 531  
 Perna, R., Lazzati, D., & Giacomazzo, B. 2016, *ApJL*, **821**, L18  
 Pittori, C. & The Agile-Ssdc Team 2019, *RLSFN*, **30**, 217  
 Prest, M., Barbiellini, G., Bordignon, G., et al. 2003, *NIMPA*, **501**, 280  
 Rezzolla, L., Giacomazzo, B., Baiotti, L., et al. 2011, *ApJL*, **732**, L6  
 Rosswog, S. 2005, *ApJ*, **634**, 1202  
 Savchenko, V., Ferrigno, C., Kuulkers, E., et al. 2017, *ApJL*, **848**, L15  
 Spruit, H. C. 1999, *A&A*, **341**, L1  
 Tavani, M. 2019, *RLSFN*, **30**, 13  
 Tavani, M., Barbiellini, G., Argan, A., et al. 2009, *A&A*, **502**, 995  
 Tavani, M., Pittori, C., Verrecchia, F., et al. 2016, *ApJL*, **825**, L4  
 Thompson, C. 1994, *MNRAS*, **270**, 480  
 Troja, E., King, A. R., O'Brien, P. T., Lyons, N., & Cusumano, G. 2008, *MNRAS*, **385**, L10  
 Ursi, A., Tavani, M., Verrecchia, F., et al. 2019, *ApJ*, **871**, 27  
 Ursi, A., Tavani, M., Verrecchia, F., et al. 2021, *ApJ*, submitted  
 Usov, V. V. 1992, *Natur*, **357**, 472  
 Verrecchia, F., Tavani, M., Bulgarelli, A., et al. 2019, *RLSFN*, **30**, 71  
 Verrecchia, F., Tavani, M., Donnarumma, I., et al. 2017a, *ApJL*, **850**, L27  
 Verrecchia, F., Tavani, M., Ursi, A., et al. 2017b, *ApJL*, **847**, L20  
 Woosley, S. E. 2016, *ApJL*, **824**, L10  
 Zhang, B. 2019, *FrPhy*, **14**, 64402  
 Zhang, B., & Mészáros, P. 2001, *ApJL*, **552**, L35